

Weyl Ferroelectric Semimetal

Ronghan Li,^{1,*} Yuanfeng Xu,^{2,*} Jianggang He,^{3,*} Sami Ullah,¹ Jiangxiu Li,¹ Jun-Ming Liu,⁴ Dianzhong Li,¹ Cesare Franchini,^{3,‡} Hongming Weng,^{2,5,‡} and Xing-Qiu Chen,^{‡,1}

¹Shenyang National Laboratory for Materials Science, Institute of Metal Research, Chinese Academy of Science, School of Materials Science and Engineering, University of Science and Technology of China, 110016 Shenyang, Liaoning, China,

²Beijing National Laboratory for Condensed Matter Physics, and Institute of Physics, Chinese Academy of Sciences, Beijing 100190, China,

³University of Vienna, Faculty of Physics and Center for Computational Materials Science, Sensegass 8/8, A-1090 Vienna, Austria,

⁴Laboratory of Solid State Microstructures and Innovation Center of Advanced Microstructures, Nanjing University, Nanjing 210093, China,

⁵Collaborative Innovation Center of Quantum Matter, Beijing, China.

(Dated: October 25, 2016)

The recent discoveries of ferroelectric metal and Weyl semimetal (WSM) have stimulated a natural question: whether these two exotic states of matter can coexist in a single material or not. These two discoveries ensure us that physically it is possible since both of them share the same necessary condition, the broken inversion symmetry. Here, by using first-principles calculations, we demonstrate that the experimentally synthesized nonmagnetic HgPbO₃ represents a unique example of such hybrid “*Weyl ferroelectric semimetal*”. Its centrosymmetric $R\bar{3}c$ phase will undergo a ferroelectric phase transition to the ferroelectric $R3c$ structure. Both phases are metallic and the ferroelectric phase owns a spontaneous polarization of 33 $\mu\text{C}/\text{cm}^2$. Most importantly, it also harbors six pairs of chiral Weyl nodes around the Fermi level to be an oxide WSM. The structural symmetry broken phase transition induces a topological phase transition. The coexistence of ferroelectricity and Weyl nodes in HgPbO₃ is an ideal platform for exploring multiphase interaction and mutual control. The Weyl nodes can be tuned by external pulse electric field, which is promising for potential applications of integrated topotronic and ferroelectric devices.

I. INTRODUCTION

Noncentrosymmetric (NCS) lattice is an important asset for hosting two seemingly incompatible phenomena: ferroelectricity and topological semimetals, such as WSM. Ferroelectricity arises from the formation of electric dipoles due to the separated centers of positive and negative charges under polar distortion, as shown in Fig. 1(a). Owing to the screening of free carriers in metals, ferroelectricity and ferroelectric phase transition are generally thought to occur only in insulators. However, in 1965 P. W. Anderson and E. I. Blount suggested that, if a structural transition occurs in a metal that is accompanied by the appearance of a polar axis and the disappearance of inversion centre, a “ferroelectric metal” can be expected¹. Indeed, ferroelectric metallic state and the ferroelectric phase transition have been recently discovered in LiOsO₃² and several other oxides^{3–5}. On the other hand, NCS WSM with time reversal symmetry have also been discovered^{6–8}. The lack of inversion center breaks the Kramer degeneracy, leading to separation of chiral Weyl nodes, which are formed by crossing of two non-degenerate bands around Fermi level. Within this context, in principle the ferroelectricity and WSMs can coexist in a single material.

Although several nonmagnetic WSMs, such as TaAs family^{9–12}, Ta₃S₂¹³, TaIrTe₄¹⁴, WTe₂^{15,16}, chemically doped KMgBi^{20–22}, chalcopyrites like CuTlSe₂¹⁷, HgTe class material¹⁸, and ZrTe¹⁹ have been proposed and partially experimentally confirmed, neither ferroelectricity nor ferroelectric phase transition has been reported. According to the space group of these crystals, the former five materials can have ferroelectricity because the electric dipole is allowed to exist, whereas the latter three cases are expected to have piezoelec-

tricity due to the nonexistence of polar axis. The ferroelectric phase transition is accompanied with the inversion symmetry breaking and, hence, it is also possible to induce topological phase transition to WSM since the inversion symmetry and time reversal symmetry result in Kramer degeneracy in bands and prevent the separation of Weyl nodes with opposite chirality.

To form ferroelectric metal it is necessary to have a finite occupation at the Fermi level and an electronic structure insensitive to polar ionic displacement in a polar lattice^{1–5}, thus ensuring that orbital-like electronic states at the Fermi level are decoupled from the polar displacement. On the other hand, the design principles for WSMs include a fully filled band at the border of a semiconducting regime and a strong spin-orbit coupling (SOC) which could cause large Rashba-like spin splitting in a NCS lattice. By combining these design principles we achieve the following criteria for the realization of coexisting Weyl nodes and ferroelectric metal: (i) a polar and flexible lattice, (ii) fully filled electron orbitals, and (iii) strong SOC. Clearly, oxides represent the most promising playground owing to their chemical and structural flexibility and to the abundance of data available in literatures^{25,28}. To fulfill the fully-filled orbital condition we adopt the simple chemical concept of electronegativity as used in our previous work²⁷. Finally, the strength of SOC can be estimated from the atomic number of the atomic constituents. We find that these conditions are simultaneously satisfied in the rhombohedral oxide HgPbO₃. Based on first-principles calculation we demonstrate that HgPbO₃ is a WSM with ferroelectric phase transition, that we name “*Weyl ferroelectric semimetal*”.

II. COMPUTATIONAL METHODS

1) **Structural optimizations and electronic band structures** The structural optimization and electronic properties were performed within the framework of the density functional theory (DFT)^{32,33} by employing the Vienna *ab initio* simulation package (VASP)^{34,35} based on the projector augmented wave (PAW) method³⁶. We have used the generalized gradient approximation of Perdew-Burke-Ernzerhof (PBE)³⁷. The adopted PAW-PBE pseudopotentials of Hg, Pb and O treat $5d^{10}6s^1$, $5d^{10}6s^26p^2$ and $2s^22p^3$ electrons as valence states. The energy cutoff was set at 500 eV and appropriate Monkhorst-Pack k meshes ($13 \times 13 \times 13$) were chosen. A very accurate criteria were used for the structural relaxation (forces < 0.0001 eV/Å). In order to double check the electronic band structures with the presence of Dirac and Weyl nodes, we have also employed the hybrid density functional theory developed by Heyd, Scuseria and Ernzerhof (HSE)^{38,39} and the GW method⁴⁰. For HSE, we have adopted the standard set-up for μ and α : $\mu = 0.20$ Å⁻¹ controls the range separation between the short-range and long-range parts of the Coulomb kernel and whereas $\alpha = 0.25$ is the mixing parameter determining the fraction of exact Hartree-Fock exchange incorporated.

2) **Phonon calculations** To inspect the dynamical stability of the ground state structure, we carried out phonon calculations. The phonon properties were computed using finite-displacements and density functional perturbation theory (DFPT)⁴², in supercells containing $2 \times 2 \times 2$ primitive cells. The phonon spectra was derived by interfacing VASP with the code Phonopy⁴¹.

3) **Surface electronic band structures** The surface state calculations have been performed using a Green's function based tight-binding (TB) approach⁴³. The TB model Hamiltonian was constructed by means of maximally-localized Wannier functions (MLWFs)^{45,46} obtained by the the Wannier90 code⁴⁴ and constructed from s -, p -, d atomic-like orbitals. The TB parameters were obtained from the MLWFs overlap matrix.

4) **Electric polarization calculations** The spontaneous electric polarization is estimated by $P_\alpha = \frac{e}{\Omega} \sum_{k,\beta} Z_{k,\alpha\beta}^* u_{k,\beta}$, using the normal charges (Z^* , Hg: +2; Pb: +4; O: -2) and atom displacements (u) of the polar structure ($R3c$) with respect to the reference phase $R\bar{3}c$, where Ω and e are the volume of the unit cell and the elementary electron charge, respectively.

III. RESULTS AND DISCUSSIONS

HgPbO₃ was synthesized in 1973 in the temperature range 600-1000 °C under 30 to 65 kbars pressure²³. Unlike the isoelectronic CdPbO₃ which was found to be a polar semiconductor^{24,25}, HgPbO₃ was reported to be black and weakly conducting ($\rho \approx 10^{-3}$ ohm/cm)²³. Experimental ambiguity on the crystal structure remains, specifically on whether HgPbO₃ is polar ($R3c$) or nonpolar ($R\bar{3}c$), see Fig. 1(a)²⁵. To clarify this issue we have conducted a direct comparison between

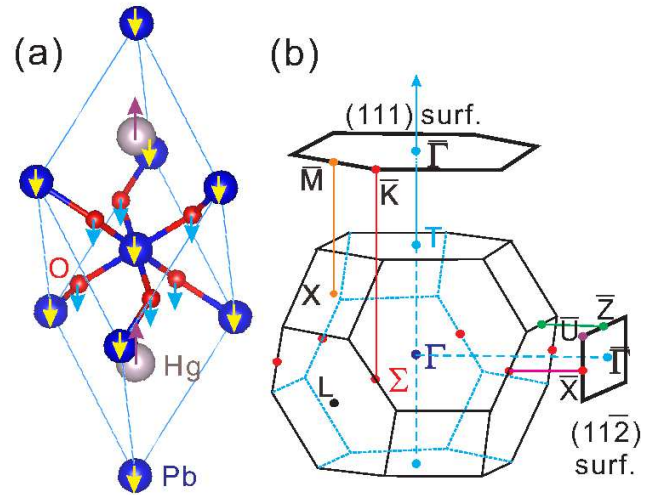


FIG. 1. **Crystal structure and Brillouin zone (BZ) of HgPbO₃.** Panel (a) denotes the unit cell of centrosymmetric $R\bar{3}c$ rhombohedral lattice. The arrows at each atom denote the atomic displacement in the softest phonon mode Γ_2^- with imaginary frequency of $1.28i$ THz at Γ in Fig. 2. Such polar distortion leads to its ferroelectric phase of $R3c$ lattice. Panel (b) shows the BZ and high symmetrical k -points of the rhombohedral lattice, as well as the projected (111) and (112) surfaces BZ.

the two phases and found that the $R3c$ phase is more stable than $R\bar{3}c$ by 3 meV/atom. Further support for this conclusion is provided by the calculated phonon dispersions. As shown in Fig. 2, the nonpolar $R\bar{3}c$ phase has imaginary frequencies whereas the polar $R3c$ phase does not have and is dynamically stable.

The most unstable phonon mode of the $R\bar{3}c$ phase is the infrared active mode of A_{2u} at Γ (Γ_2^-), which involves the cooperative displacements of the negatively charged oxygen ions opposite to the positively charged Hg and Pb cations along the c -axis of the hexagonal lattice, or equivalently the $\langle 111 \rangle$ direction of rhombohedral lattice, as shown in Fig. 1. By freezing the Γ_2^- mode at different amplitude, the centrosymmetric $R\bar{3}c$ lattice is shown to be transformed into the polar $R3c$ lattice with energy gain of 3 meV/atom (Fig. 2c) at the ground state. All of these distorted crystals are metallic in their band structure, reflecting well the experimentally measured weak conductivity²³. By using the normal charges of cations and anion (Hg: +2; Pb: +4; O: -2), the estimated spontaneous polarization along the polar axis c is as high as $33 \mu\text{C}/\text{cm}^2$. The rather small energy change (3 meV/atom) during this process implies an accessible ferroelectric phase transition with decreasing temperature. This is consistent with the analysis of Anderson and Blount¹ for the identification of a ferroelectric metal. Similar to the prototype ferroelectric metal LiOsO₃, the main polar distortion arises from opposite displacements of the A -site cation (Hg) (0.37 Å) and O atoms (0.27 Å) along the c -axis. The B -site (Pb) cation has the smallest displacement (0.1 Å). Considering the large polar distortion (0.53 Å amplitude of Γ_2^- mode), small energy difference ΔE between the

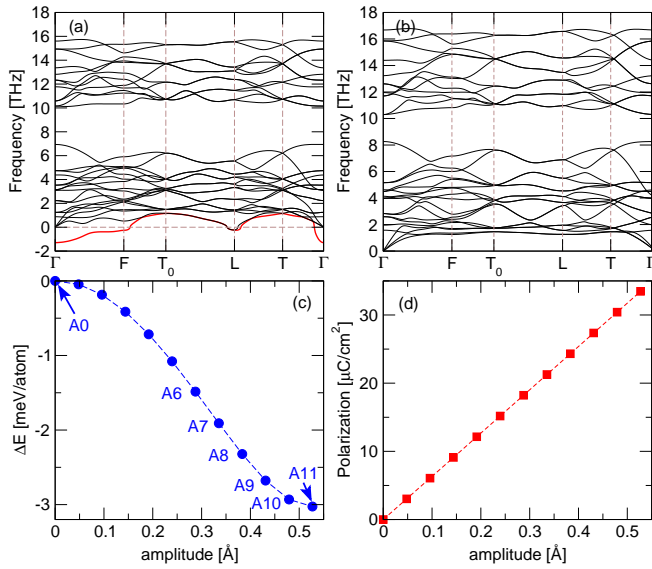


FIG. 2. **Phonons and ferroelectric distortion of HgPbO_3 .** Calculated phonon dispersions for the nonpolar $R\bar{3}c$ (a) and polar $R3c$ (b) structures. (c) The energy difference ΔE between the polar and nonpolar phases and (d) the electric polarization P as a function of the amplitude (A0, ..., A11) of the frozen polar mode Γ_2^- .

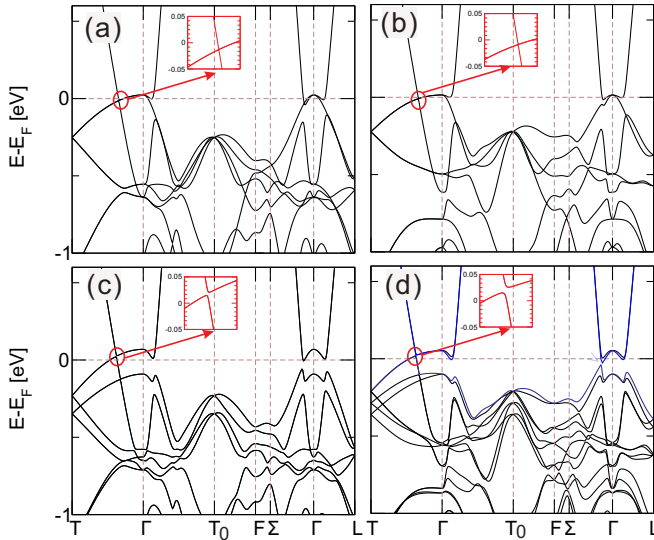


FIG. 3. **Calculated electronic band structures of HgPbO_3 .** Panels (a) and (b) are those calculated without SOC for the nonpolar $R\bar{3}c$ and polar $R3c$ phases, respectively. Panels (c) and (d) are the corresponding ones with SOC included. The insets stress the crossing (without SOC) and anti-crossing (with SOC) of the bands mainly composed of $6s$ orbitals of Hg and Pb atoms and $2p$ orbitals of oxygen atoms.

polar and nonpolar phase, and weak screening in semimetal of low carrier density, the polar ground state is expected to be tunable by applying suitable pulse electric field opposite to the 'spontaneous polarization'.

The inspection of the electronic structures shows that in HgPdO_3 the ferroelectric instability is coupled with striking

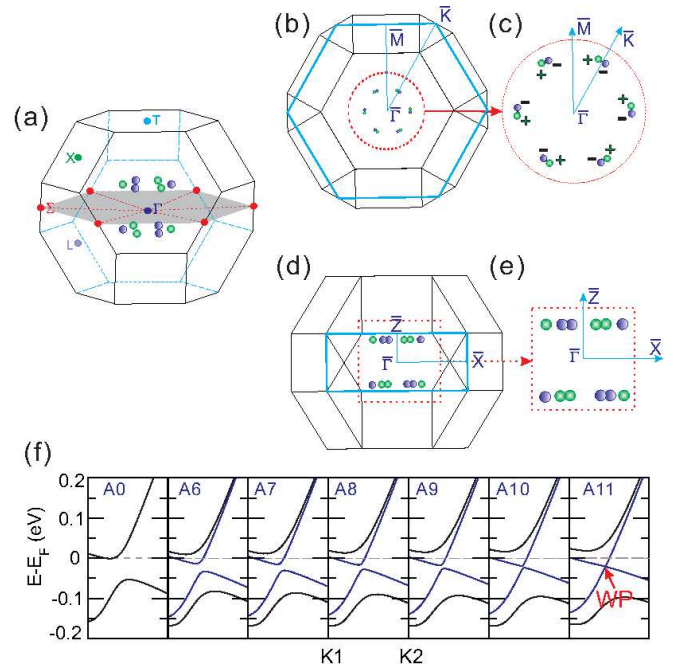


FIG. 4. **Weyl nodes and their distribution in the BZ of the most stable ferroelectric $R3c$ HgPbO_3 .** One of the Weyl node is at $(0.15273470, 0.06175918, -0.01762040)$ and all the others can be obtained by imposing crystal and time-reversal symmetries (see the supplementary Table S1). Panel (a): three-dimensional visualization of the Weyl nodes in the BZ, (b) two-dimensional projection along the $\langle 111 \rangle$ direction and the panel (c) is the enlarged plot of the projected Weyl nodes, and (d) two-dimensional projection along the $\langle 11\bar{2} \rangle$ direction and the panel (e) is the enlarged plot of the projected Weyl nodes. The green and blue points denote the opposite chirality of the corresponding nodes. Panel (f) shows the changes in the band structure at one Weyl node as the function of the amplitude of polar distortion (A0, ..., A11 as labeled in Fig. 2c) along the path parallel with the $\bar{\Gamma}-\bar{K}$.

topological phase transition from a normal semimetal to a WSM with Weyl nodes, as evidenced in Figs. 3 and 4. By neglecting the SOC, the band structure of the $R\bar{3}c$ and $R3c$ phases are very similar, characterized by a band crossing around the Fermi level along the Γ -T direction. One of the band is a nondegenerate band mainly composed of $6s$ orbitals from Hg and Pb atoms, while the others are double degenerate bands mostly of oxygen atoms' $2p$ orbitals. Such s - p band inversion (supplementary Fig. S1) leads to a triply degenerate nodal point along Γ -T, similar to that in TaN and others^{19,29,30}. However, such triply degenerated nodal point becomes gaped once SOC is further included. In the polar $R3c$ case, the gap is about 7 meV and in the centrosymmetric $R\bar{3}c$ case the gap is smaller, about 5 meV. It needs to be emphasized that electronic structure obtained using the more accurate hybrid functionals (HSE) and GW methods is almost identical to the DFT one (supplemental Fig. S2 and Fig. S3). Another most important difference between these two phases is that the Kramer degeneracy is broken in ferroelectric one. The Rashba like splitting can be clearly seen when compar-

ing the bands around Γ along either Γ - Σ or Γ - L . This might lead to appearance of separated chiral Weyl nodes in NCS polar $R3c$ phase. And indeed, we have identified that there are totally six pairs of Weyl nodes in the first BZ as shown in Fig. 4. Each of them is related with the others by C_3 rotational symmetry around the c axis, the mirror symmetries with mirror planes passing through Γ -T and Γ -L, and the time-reversal symmetry. The energy of the Weyl node is around 22 meV below the Fermi level. The exact position and the chirality of these Weyl nodes are specified in supplementary Table S1. The Weyl cone shape can be seen from the energy dispersions along several different directions as shown in supplementary Fig.S4. Again, we monitor the evolution of band structure around one Weyl node as the amplitude of the polar distortion of Γ_2^- soft mode changes. As clearly shown in Fig. 4, the topological phase transition happens during the ferroelectric phase transition. Thus, we have identified an unusual and tunable coupling between topological Weyl fermion and the ferroelectric properties.

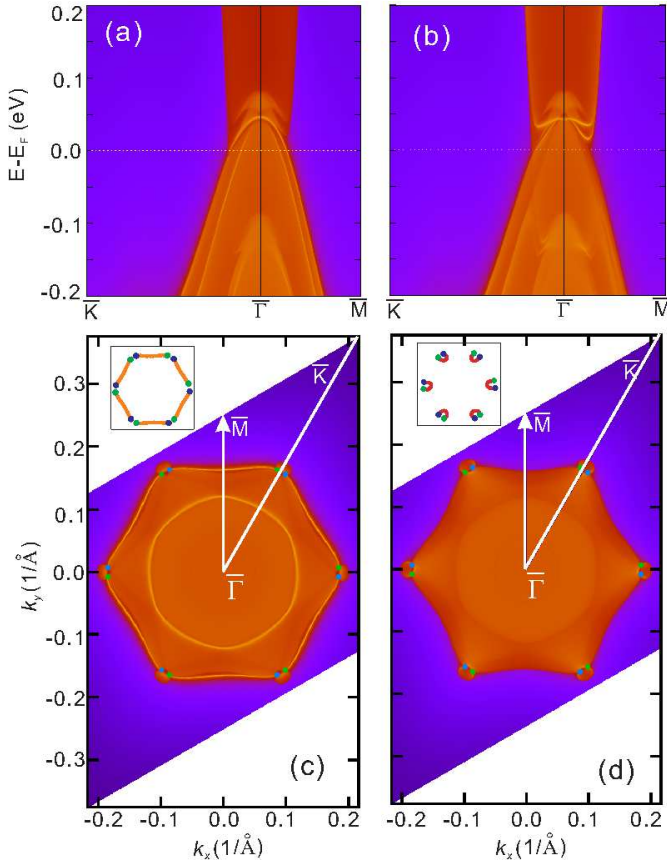


FIG. 5. Calculated (111) surface state of the polar $R3c$ HgPbO_3 . Panels (a) and (b) are the band structures of the top and bottom surfaces, respectively. Panels (c) and (d) are the Fermi surfaces at -22 meV below the Fermi level in panels (a) and (b), respectively. Insets in (c) and (d) show the Fermi arc pattern. Blue and green points are the surface projections of the Weyl nodes of the opposite chirality.

WSM often exhibits nontrivial surface states^{7,8}, such as Fermi arcs. To inspect them for the ferroelectric HgPbO_3 , we calculate the surface electronic band structures within the

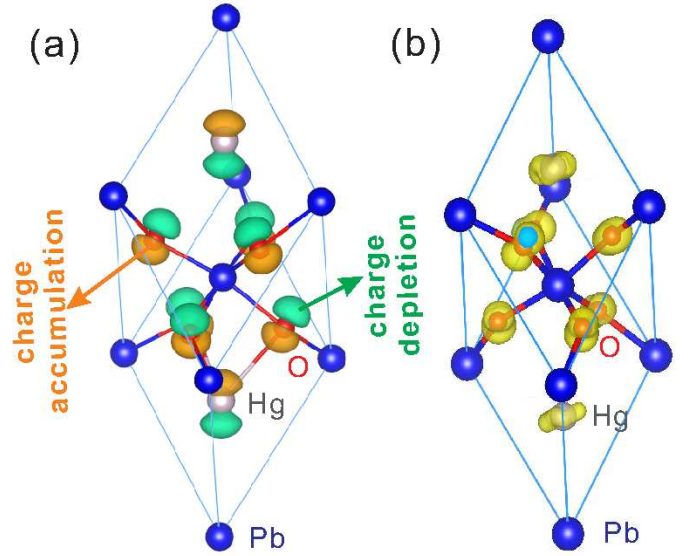


FIG. 6. Localized charges associated with local electric dipoles and Weyl carriers of the polar $R3c$ HgPbO_3 . Panel (a) Charge distribution difference, $\Delta\rho = \rho_{R3c} - \rho_{R3c\bar{c}}$, between that of the polar $R3c$ (ρ_{R3c}) and nonpolar $R3c\bar{c}$ ($\rho_{R3c\bar{c}}$) structure of HgPbO_3 . (b) Distribution of the carriers in the electron-pockets containing Weyl nodes. The orange and green colors denote the charge accumulation and depletion, respectively. It is clearly to see that the $\Delta\rho$ on Hg and O are accumulated and depleted in the opposite direction to form dipole moment because of the polar displacement.

tight-binding model based Green's function method. The Wannier functions are generated from the the bulk Hg 6s, Hg 5d, Pb 6s and O 2p orbitals as the basis set of tight-binding model. Fig. 5 shows the (111) surface band structures and their corresponding Fermi surfaces at the energy of Weyl nodes for the top and bottom surfaces. As illustrated in Fig. 5a and 5b, the projected Weyl nodes are hidden by the other overlapped bulk states. But there are still some surface states with quite high surface local density of states can be identified. Fig. 5c and 5d are the plotting of Fermi surface with chemical potential at Weyl nodes. The Fermi arcs connecting the projection of the Weyl nodes with opposite chirality are well resolved for both top and bottom surfaces. We have also checked the surface electronic bands on the (112) top and bottom surfaces, perpendicular to the (111) surface (see supplementary Fig. S5(a and b)). However, all these projected Weyl nodes on the (112) surface still overlaps the bulk bands as illustrated in supplementary Fig. S5(c and d).

Finally, to reveal the underlying mechanism of the coexistence between WSM and ferroelectricity in HgPbO_3 , we find that the charges at the Weyl nodes mainly contribute to well localized charge redistribution associated with the formation of local dipole moments, as shown in Fig. 6. It is clear that ferroelectric-like phases are not expected to form in metals, mainly because the screening potential imposed by free electrons in metals prevents the electric dipoles from feeling each other and, hence, stops them from aligning in order²⁶. However, compared to standard metals, WSM appear to be a more

suitable platform to host ferroelectric metal, since the charge carriers in Weyl nodes predominantly move along the linearly dispersive bands forming the nodes. Due to this confinement, Weyl carriers are not expected to be easily redistributed in all the lattice space but localized on the orbitals composing the linear bands. This is different from the nearly free electrons with parabolic band dispersion in normal metals, where the electrons can travel over all the lattice space to be extended. Moreover, the strength of electrostatic screening in WSM is much weaker than the normal metal due to the much lower carrier density. Therefore, if a NCS lattice of WSM is flexible enough to allow the cooperative atomic displacement with the positively and negatively charged ions to form electric dipoles in a proper ferroelectric pattern, this most probably will form a Weyl ferroelectric semimetals.

IV. CONCLUSIONS

In conclusion, we have shown that HgPbO_3 is a semimetal with ferroelectric phase transition and its dynamically stable $R3c$ phase has dipole moment. Notably, such ferroelectric metal possesses six pairs of Weyl nodes, which represents the first example of an oxide Weyl ferroelectric semimetal. The Weyl nodes can be selectively tuned by applying an external pulse electric field, implying potential applications as quantum switch in processing devices. The coexistence and the coupling between WSM phase and the ferroelectric phase transition, assisted by strong relativistic effects in a NCS back-

ground, has been achieved by judicious material design based on well-defined building criteria. It represents a unique feature never observed hitherto in known Weyl semimetals³¹ and ferroelectric metals⁵. This opens the way to novel quantum devices based on topological multifunctional materials.

Acknowledgments Work in IMR, China, was supported by the ‘‘Hundred Talents Project’’ of the Chinese Academy of Sciences and the Major Research Plan (Grant No. 91226204), the Key Research Program of CAS (Grant No. KGZD-EW-T06), the National Natural Science Foundation of China (Grant Nos. 51671193, 51474202 and 51431006) and the computational resources from the national supercomputer center (TH-2A). Y. X. and H.M.W in IOP, China, are supported by the National 973 program of China (Grant No. 2013CB921700), the ‘‘Strategic Priority Research Program (B)’’ of the Chinese Academy of Sciences (Grant No. XDB07020100), the MOST project under the contract number 2016YFA0300604 and the National Natural Science Foundation of China (Grant Nos. 11274359, 11422428 and 11674369). C.F. acknowledges support by the Austrian Science Fund (FWF) project INDOX (I1490-N19) and ViCoM (Grant No. F41). Calculations in Vienna were performed in the Vienna Scientific Cluster.

*These authors contributed equally to this work.

‡ Corresponding author:

xingqiu.chen@imr.ac.cn (X.-Q. C.),
cesare.franchini@univie.ac.at (C. F.),
hmweng@iphy.ac.cn (H. M. W.)

-
- ¹ P. W. Anderson and E. I. Blount, Symmetry considerations on martensitic transformations: ‘‘ferroelectric metals?’’, *Phys. Rev. Lett.*, **14**, 217-219 (1965).
 - ² Y. G. Shi, Y. F. Guo, X. Wang, A. J. Princep, D. Khalyavin, P. Manuel, Y. C. Michiue, A. Sato, K. J. Tsuda, S. Yu, M. Arai, Y. Shirako, M. Akaogi, N. L. Wang, K. Yamaura, and A. T. Boothroyd, A ferroelectric-like structural transition in a metal, *Nature Mater.*, **12**, 1024-1027 (2013).
 - ³ J. T. Vaughey, J. P. Thiel, E. F. Hasty, D. A. Groenke, Charlotte L. Stern, K. R. Poeppelmeier, B. Dabrowski, D. G. Hinks, and A. W. Mitchell, Synthesis and structure of a new family of cuprate superconductors: $\text{LnSr}_2\text{Cu}_2\text{GaO}_7$, *Chem. Mater.*, **3**, 935-940 (1991).
 - ⁴ D. Puggioni and J. M. Rondinelli, Designing a robustly metallic noncentrosymmetric ruthenate oxide with large thermopower anisotropy, *Nature Commun.*, **5**, 3432, (2014).
 - ⁵ T. H. Kim, D. Puggioni, Y. Yuan, L. Xie, H. Zhou, N. Campbell, P. J. Ryan, Y. Choi, J.-W. Kim, J. R. Patzner, S. Ryu, J. P. Podkaminer, J. Irwin, Y. Ma, C. J. Fennie, M. S. Rzechowski, X. Q. Pan, V. Gopalan, J. M. Rondinelli, and C. B. Eom, *Polar materials by geometric design*, *Nature*, **533**, 68-72 (2016).
 - ⁶ X. Wan, A. M. Turner, A. Vishwanath, and S. Y. Sarvarsov, Topological semimetal and Fermi-arc surface states in the electronic structure of pyrochlore iridates, *Phys. Rev. B*, **83**, 205101 (2011).
 - ⁷ H.M. Weng, X. Dai, and Z. Fang, Topological semimetals predicted from first-principles calculations, *J. Phys.: Condens. Matter.*, **28**, 303001 (2016).
 - ⁸ M. Z. Hasan, S.-Y. Xu, and G. Bian, Topological insulators, topological superconductors and Weyl fermion semimetals: discoveries, perspectives and outlooks, *Phys. Scr.*, **T164**, 014001 (2015).
 - ⁹ H. M. Weng, C. Fang, Z. Fang, B. A. Bernevig, and X. Dai, Weyl Semimetal Phase in Noncentrosymmetric Transition-Metal Monophosphides, *Phys. Rev. X*, **5**, 011029 (2015).
 - ¹⁰ S. M. Huang, S. Y. Xu, I. Belopolski, C. C. Lee, G. Q. Chang, B. K. Wang, N. Alidoust, G. Bian, M. Neupane, C. L. Zhang, S. Jia, A. Bansil, H. Lin, and M. Z. Hasan, A Weyl Fermion semimetal with surface Fermi arcs in the transition metal monopnictide TaAs class, *Nature Commun.*, **6**, 7373 (2015).
 - ¹¹ B. Q. Lv, H. M. Weng, B. B. Fu, X. P. Wang, H. Miao, J. Ma, P. Richard, X. C. Huang, L. X. Zhao, G. F. Chen, Z. Fang, X. Dai, T. Qian, and H. Ding, Experimental Discovery of Weyl Semimetal TaAs, *Phys. Rev. X*, **5**, 031013 (2015).
 - ¹² S. Y. Xu, I. Belopolski, N. Alidoust, M. Neupane, G. Bian, C. L. Zhang, R. Sankar, G. Q. Chang, Z. J. Yuan, C. C. Lee, S. M. Huang, H. Zheng, J. Ma, D. S. Sanchez, B. K. Wang, A. Bansil, F. C. Chou, P. P. Shibayev, H. Lin, S. Jia, and M. Z. Hasan, Discovery of a Weyl fermion semimetal and topological Fermi arcs, *Science*, **349**, 613-617 (2015).
 - ¹³ G. Q. Chang, S.-Y. Xu, D. S. Sanchez, S.-M. Huang, C.-C. Lee, T.-R. Chang, G. Bian, H. Zheng, I. Belopolski, N. Alidoust, H.-T. Jeng, A. Bansil, H. Lin, and M. Z. Hasan, A strongly robust type II Weyl fermion semimetal state in Ta_3S_2 , *Science Advances*, **2**, e1600295 (2016).
 - ¹⁴ K. Koepnik, D. Kashinathan, D. V. Efremov, S. Khim, S. Borisenko, B. Büchner, and J. van den Brink, TaIrTe_4 : A ternary type-II Weyl semimetal, *Phys. Rev. B*, **93**, 201101(R), (2016).
 - ¹⁵ A. A. Soluyanov, D. Gresch, Z. J. Wang, Q. S. Wu, M. Troyer, X.

- Dai, and B. A. Bernevig, Type-II Weyl semimetals, *Nature*, **527**, 495-499 (2015).
- ¹⁶ F.-Y. Li, X. Luo, X. Dai, Y. Yu, F. Zhang, and G. Chen, Hybrid Weyl Semimetal, arxiv: 1607.08474 (2016).
- ¹⁷ J. W. Ruan, S.-K. Jian, D.Q. Zhang, H. Yao, H.J. Zhang, S.-C. Zhang, and D. Y. Xing, Ideal Weyl semimetals in the Chalcopyrites CuTiSe_2 , AgTlTe_2 , AuTlTe_2 , and ZnPbAs_2 , *Phys. Rev. Lett.*, **116**, 226801 (2016).
- ¹⁸ J. W. Ruan, S.-K. Jian, H. Yao, S.-C. Zhang, D. Y. Xing, Symmetry-protected ideal Weyl semimetal in HgTe-class materials, *Nature Communications*, **7**, 11136 (2016).
- ¹⁹ H.M. Weng, C. Fang, Z. Fang and X. Dai, Coexistence of Weyl fermion and massless triply degenerate nodal points, *Phys. Rev. B* **94**, 165201 (2016).
- ²⁰ K. F. Carrity, K. M. Rabe, and D. Vanderbilt, Hyperferroelectrics: Proper Ferroelectrics with Persistent Polarization, *Phys. Rev. Lett.*, **112**, 127601 (2014).
- ²¹ D. D. Sante, P. Barone, A. Stroppa, K. F. Carrity, D. Vanderbilt and S. Picozzi, Intertwined Rashba, Dirac and Weyl Fermions in Hexagonal Hyperferroelectrics, *Phys. Rev. Lett.*, **117**, 076401 (2016).
- ²² A. Narayan, Class of Rashba ferroelectrics in hexagonal semiconductors, *Phys. Rev. B*, **92**, 220101(R), (2015).
- ²³ A. W. Sleight and C. P. Prewitt, High-pressure HgTiO_3 and HgPbO_3 : Preparation, characterization, and structure, *J. Solid State Chem.* **6**, 509 (1973).
- ²⁴ H. S. Nabi, R. Pentcheva and R. Ranjan, Ab initio electronic structures of rhombohedral and cubic HgXO_3 ($X = \text{Ti}, \text{Pb}$), *J. Phys.: Condens. Matter* **22**, 045504 (2010).
- ²⁵ J. G. He, C. Franchini, and J. M. Rondinelli, Lithium Niobate-type oxides as visible light photovoltaic materials, *Chem. Mater.*, **28**, 25-29 (2016).
- ²⁶ M. Ležaić, Clockwork at the atomic scale, *Nature*, **533**, 38-39 (2016).
- ²⁷ R.H. Li, Q. Xie, X.Y. Cheng, D.Z. Li, Y.Y. Li, and X.-Q. Chen, First-principles study of the large-gap three-dimensional topological insulators $M_3\text{Bi}_2$ ($M = \text{Ca}, \text{Sr}, \text{Ba}$), *Phys. Rev. B* **92**, 205130 (2015).
- ²⁸ P. S. Halasyamani and K. P. Poepelmeier, Noncentrosymmetric oxides, *Chem. Mater.*, **10**, 2753-2769 (1998).
- ²⁹ H.M. Weng, C. Fang, Z. Fang and X. Dai, Topological semimetals with triply degenerate nodal points in θ -phase tantalum nitride, *Phys. Rev. B* **93**, 241202 (2016).
- ³⁰ Z.M. Zhu, G. W. Winkler, Q.S. Wu, J. Li, and A. A. Soluyanov, Triple Point Topological Metals, *Phys. Rev. X* **6**, 031003 (2016).
- ³¹ B. Bradlyn, J. Cano, Z.J. Wang, M. G. Vergniory, C. Felser, R. J. Cava, and B. A. Bernevig, Beyond Dirac and Weyl fermions: Unconventional quasiparticles in conventional crystals, *Science*, **353**, 558 (2016).
- ³² P. Hohenberg, and W. Kohn, Inhomogeneous Electron Gas, *Phys. Rev.* **136**, B864 (1964).
- ³³ W. Kohn, and L.J. Sham, Self-Consistent Equations Including Exchange and Correlation Effects, *Phys. Rev.* **140**, A1133 (1965).
- ³⁴ G. Kresse and J. Hafner, Ab initio molecular dynamics for liquid metals, *Phys. Rev. B* **47**, 558 (1993).
- ³⁵ G. Kresse and J. Furthmüller, *Comput. Mater. Sci.* **6**, 15 (1996).
- ³⁶ P. Blöchl, Projector augmented-wave method, *Phys. Rev. B* **50**, 17953 (1994).
- ³⁷ J. Perdew, K. Burke, and M. Ernzerhof, Generalized Gradient Approximation Made Simple, *Phys. Rev. Lett.* **77**, 3865 (1996).
- ³⁸ J. Paier, M. Marsman, and G. Kresse, Why does the B3LYP hybrid functional fail for metals? *J. Chem. Phys.* **127**, 024103 (2007).
- ³⁹ J. Heyd, G. E. Scuseria, and M. Ernzerhof, Hybrid functionals based on a screened Coulomb potential, **118**, 8207 (2003).
- ⁴⁰ F. Bruneval, F. Sottile, V. Olevano, R. D. Sole, and L. Reining, Many-body perturbation theory using the density-functional concept: beyond the GW approximation. *Phys. Rev. Lett.*, **94**, 186402 (2005).
- ⁴¹ A. Togo, F. Oba, and I. Tanaka, First-principles calculations of the ferroelastic transition between rutile-type and CaCl_2 -type SiO_2 at high pressures, *Phys. Rev. B* **78**, 134106 (2008).
- ⁴² S. Baroni, S. de Gironcoli, A. D. Corso, and P. Giannozzi, Phonons and related crystal properties from density-functional perturbation theory, *Rev. Mod. Phys.* **73**, 515 (2001).
- ⁴³ M. P. Sancho, J. M. Sancho, and J. Rubio, Highly convergent schemes for the calculation of bulk and surface Green functions, *J. Phys. F: Met. Phys.* **15**, 851 (1985).
- ⁴⁴ A. A. Mostofi, J. R. Yates, Y.-S. Lee, I. Souza, D. Vanderbilt, and N. Marzari, Wannier90: A tool for obtaining maximally-localised Wannier functions, *Comput. Phys. Commun.* **178**, 685 (2008).
- ⁴⁵ N. Marzari and D. Vanderbilt, Maximally localized generalized Wannier functions for composite energy bands, *Phys. Rev. B* **56**, 12847 (1997).
- ⁴⁶ I. Souza, N. Marzari, and D. Vanderbilt, Maximally localized Wannier functions for entangled energy bands, *Phys. Rev. B*, **65**, 035109 (2001).
- ⁴⁷ C. Franchini, R. Kováčik, M. Marsman, S. Sathyanarayana Murthy, J. He, C. Ederer, and G. Kresse, Maximally localized Wannier functions in LaMnO_3 within PBE+ U , hybrid functionals and partially self-consistent GW: an efficient route to construct ab initio tight-binding parameters for perovskites. *J. Phys. Condens. Matter* **24**, 235602 (2012).

TABLE I. Supplementary Table S1: Positions and chirality of six pairs of Weyl nodes in the first Brillouin zone. The position (k_x, k_y, k_z) are in units of reciprocal lattices. All of them are related by crystal and time-reversal symmetries.

Weyl point	k_x	k_y	k_z	Chirality
W1	0.15273470	0.06175918	-0.01762040	-
W2	0.01762040	-0.06175918	-0.15273470	+
W3	-0.01762040	0.15273469	0.06175918	-
W4	-0.15273470	0.01762040	-0.06175918	+
W5	0.06175918	-0.01762040	0.15273469	-
W6	-0.06175918	-0.15273649	0.01762040	+
W7	-0.15273469	-0.06175918	0.01762040	-
W8	-0.01762040	0.06175918	0.15273469	+
W9	0.01762040	-0.15273649	-0.06175180	-
W10	0.15273469	-0.01762040	0.06175918	+
W11	-0.06175918	0.01762040	-0.15273469	-
W12	0.06175918	0.15273469	-0.01762040	+

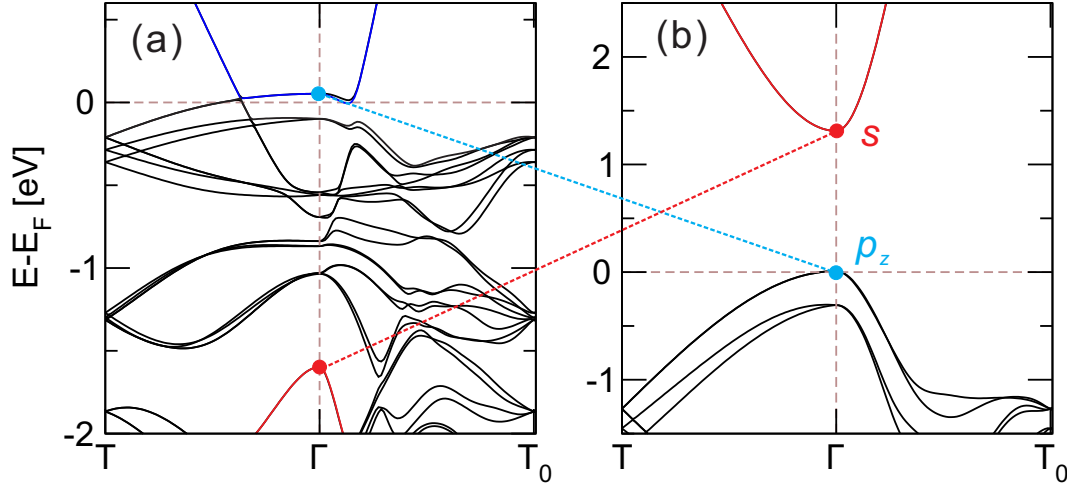


FIG. 7. Supplementary Fig.S1. $s \rightarrow p$ band inversion. To elucidate band inversion mechanism, we have analyzed the band sequences of the $R3c$ -type HgPbO_3 at the equilibrium state (a) in comparison with the artificial state by reducing the volume to 50% of the equilibrium volume. It can be seen that, at the equilibrium state the band structure shows a semimetal, whereas at the reduced volume it becomes an insulator. In the meanwhile, the band inversion occurs between the s -like orbitals from Hg and Pb atoms and the p -like orbitals from oxygen atoms.

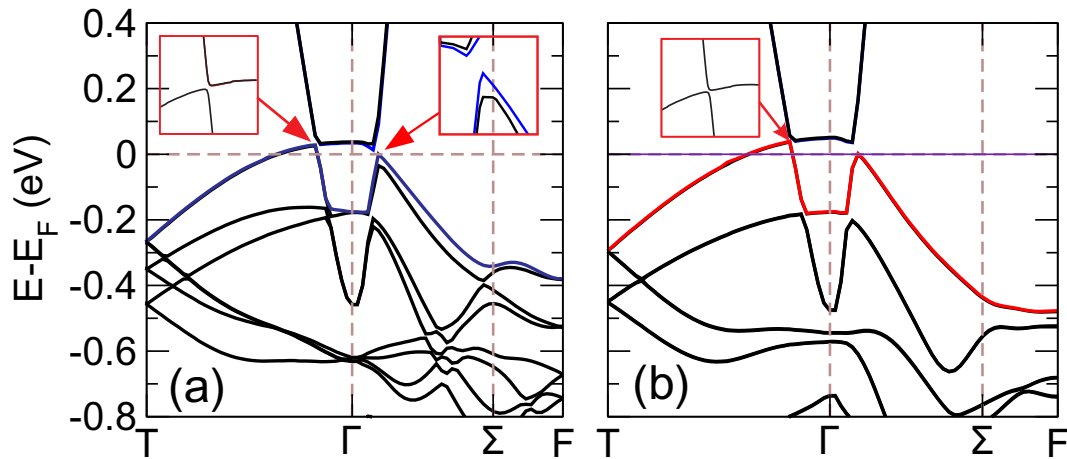


FIG. 8. Supplementary Fig.S2. **HSE derived electronic band structures of HgPbO_3 .** Due to the well-known false-positive problem of standard DFT calculations, HSE method with SOC has been performed to check whether the topologically non-trivial states in HgPbO_3 still exists when a more accurate exchange-correlation functional is introduced. The derived band structure of the NCS $R3c$ and centrosymmetric $R3c$ structures in (a) and (b), respectively, are very similarity to the DFT calculations.

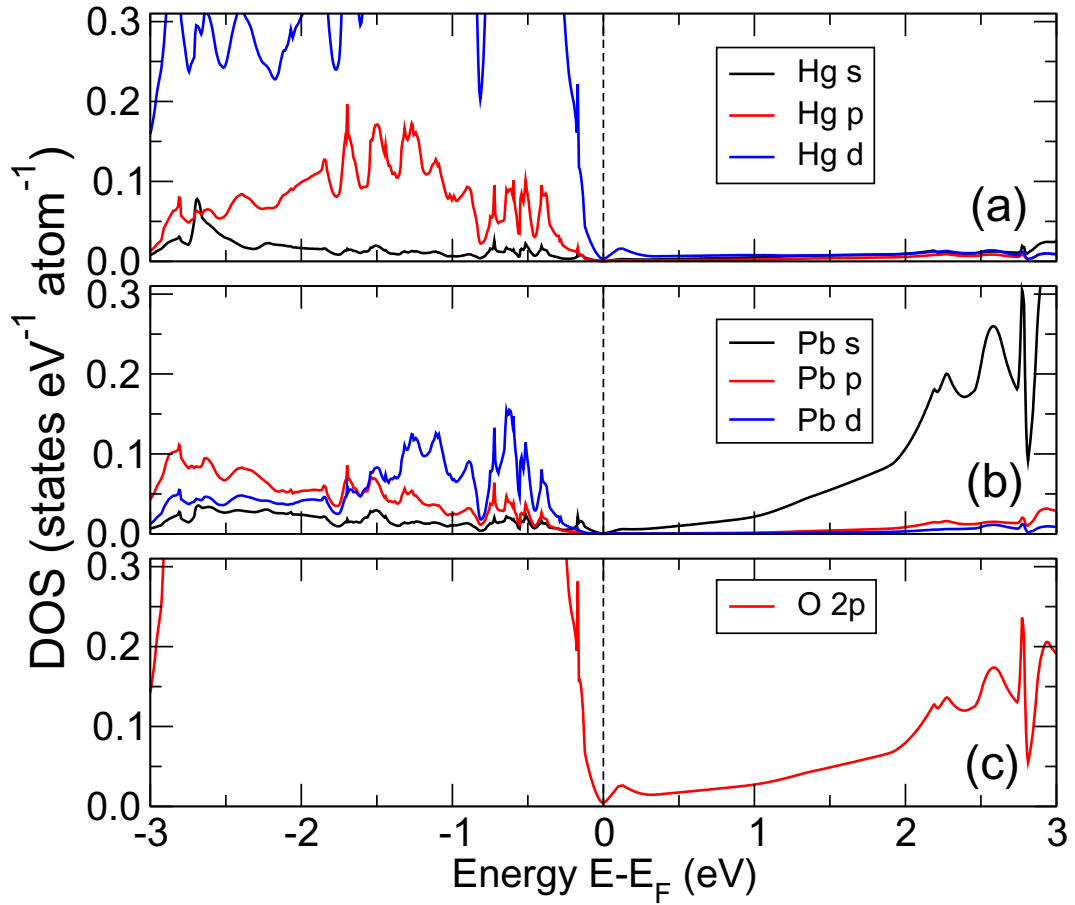


FIG. 9. Supplementary Fig.S3. **GW derived electronic densities of states (DOSs) of $R3c$ HgPbO_3 .** Because HgPbO_3 is semimetal, the GW method is not a most proper method to derive its electronic band structures. However, according to our calculations, the GW method still revealed that the GW DOSs show a clear sign of the semimetal feature, as evidenced by a highly low density at the Fermi level.

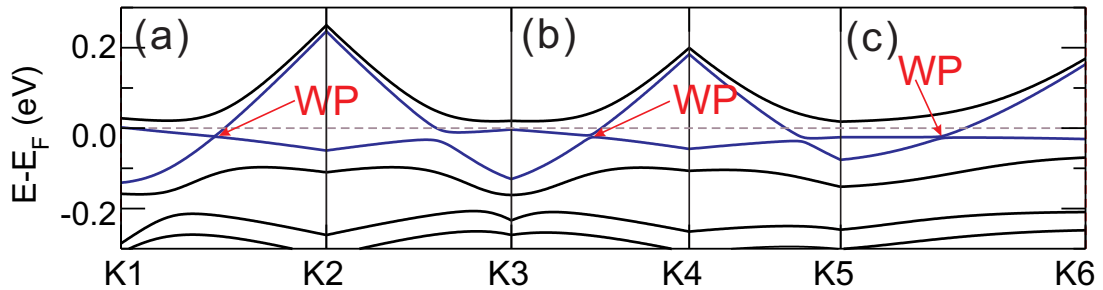


FIG. 10. Supplementary Fig.S4. **Calculated band structure along three directions passing through one Weyl node in the polar $R3c$ phase of HgPbO_3 .** Panels (a), (b) and (c) are those with k -path parallel to $\bar{\Gamma}-\bar{K}$, $\bar{\Gamma}-\bar{M}$ and $\Gamma-T$, respectively.

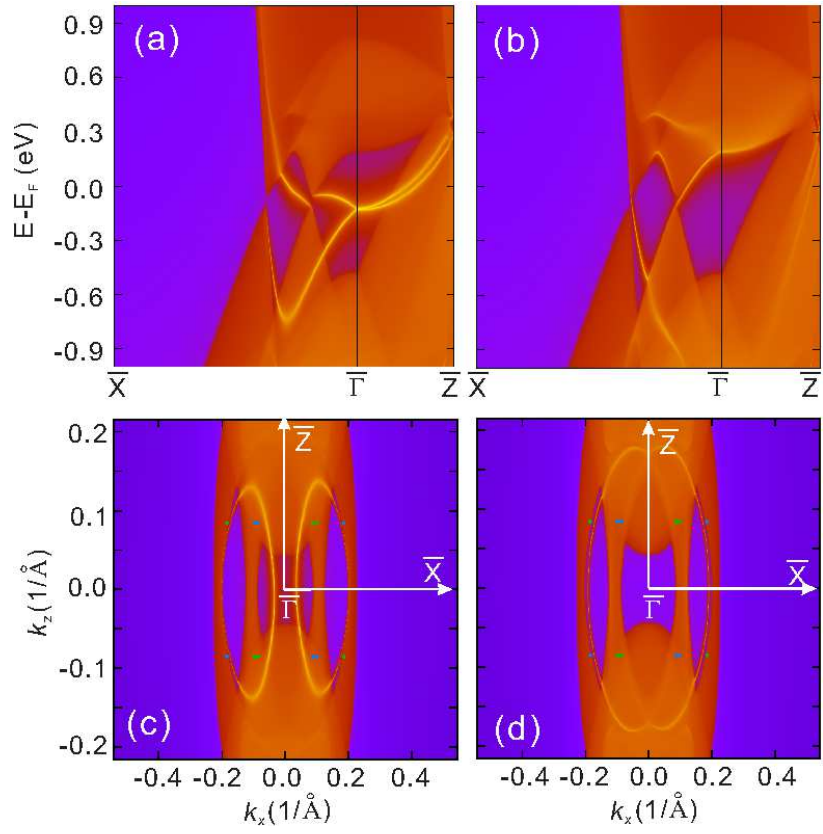


FIG. 11. Supplementary Fig.S5. Calculated $(11\bar{2})$ surface electron structures for the polar $R3c$ phase of HgPbO_3 . Panels (a) and (b) are the calculated band structures of the top and bottom surfaces, respectively. Panels (c) and (d) are the Fermi surfaces at -22 meV below the Fermi level in panels (a) and (b), respectively. Blue and green points are the surface projections of the Weyl nodes of the opposite chirality.